34

Iterative Reconstruction Methods in X-ray CT

Geert Van Eyndhoven and Jan Sijbers

CONTENTS

34.1 Introduction

In this chapter, a short introduction to computed tomography (CT) and X-ray physics is given. CT is an advanced imaging technique that allows for non-invasive visualization of the interior of a scanned object. In Figure 34.1, the typical steps involved in CT imaging are described. In a first step (see Figure 34.1a) X-ray projection images (also known as Röntgen photos or radiographs) are acquired at different angles from an object of interest. All steps involved in this acquisition process are described in Section 34.2. The second step in CT imaging is the reconstruction step, which is conceptually visualized in Figure 34.1b and thoroughly explained in Section 34.3. Finally, in Section 34.4, the concepts of the previous section are extended to dynamic CT, where the object is no longer assumed to be stationary throughout the acquisition process.

The chapter starts with a basic introduction to tomography. A more detailed overview of tomography can be found in Kak and Slaney (2001) and Buzug (2008) (see also Section III, Chapter 32, for a general introduction to CT diagnostic imaging).

34.2 Acquisition Process

In this section, a brief introduction to the CT acquisition process is given. First, in Section 34.2.1, the necessary X-ray physics are discussed. A description of the law of Beer–Lambert, which is a simple model for the data acquisition step, is given in Section 34.2.2. Finally, in Section 34.2.3, different projection geometries are discussed.

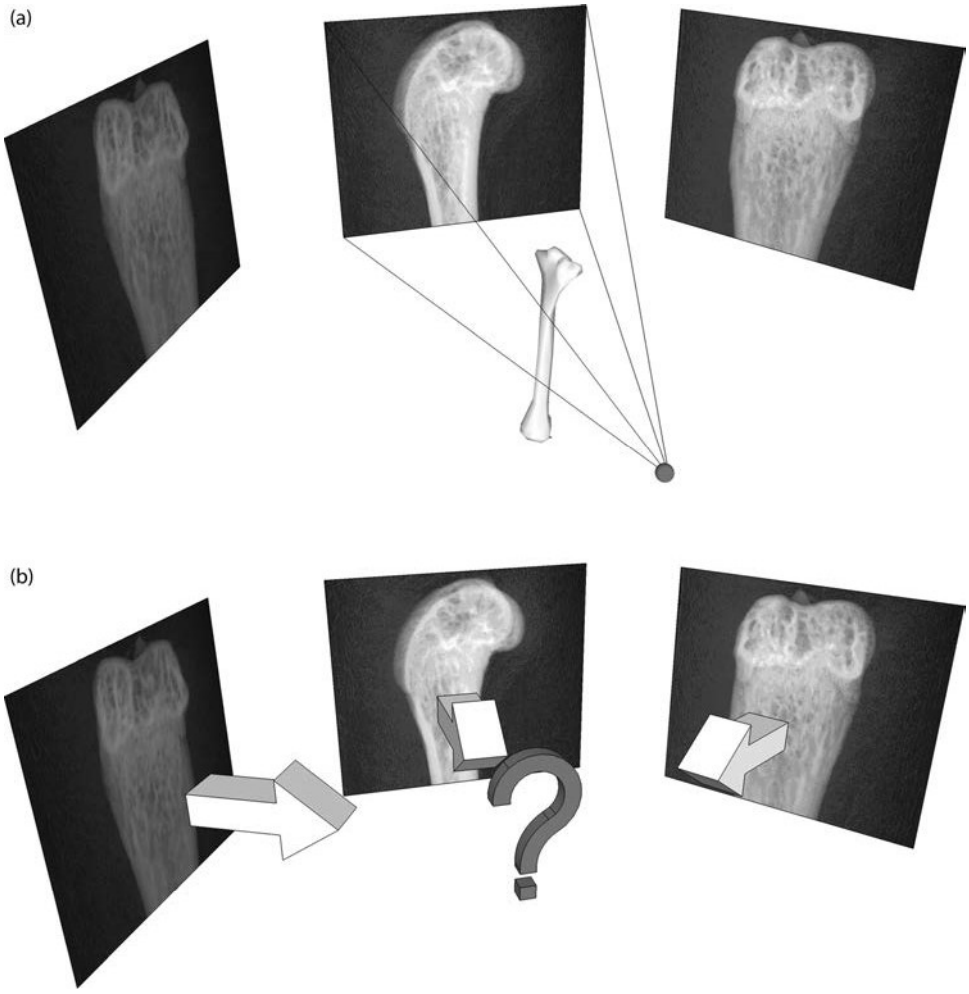

FIGURE 34.1 A conceptual visualization of forward and back-projection in X-ray CT. (a) The first step: projection data is acquired at different angles from an object under interest. (b) The second step: from the projection data, the unknown attenuation values of the object are to be calculated.

34.2.1 X-rays: Generation, Matter Interaction, and Detection

X-rays are basically electromagnetic waves with an energy range between 10 and 200 keV. They were first discovered by Wilhem Röntgen in 1895, who named it X-radiation to signify the (at that time) unknown type of radiation (Röntgen 1898) (see also Section II, Chapter 17, for an historical article on the discovery of X-rays). X-rays can be described with a wave model or a particle model. In this chapter, X-rays will be modeled as packets of energy, referred to as *photons* or X-ray *quanta*.

34.2.1.1 X-ray Generation

In medical and μCT scanners, X-rays are typically generated within a vacuum tube (see also Section I, Chapter 2, for a description of X-ray tubes). A standard vacuum tube consists of a cathode and an anode, over which a high voltage is applied. Thermionic emission sets electrons free from the cathode, accelerating them through the high voltage such that they hit the anode surface at high speed. When the fast electrons enter the anode surface, multiple interactions take place, resulting in a conversion of the electron kinetic energy into X-ray radiation and heat. The emitted X-rays have a spectrum that typically resembles the spectrum illustrated in Figure 34.2 (Buzug 2008; Duisterwinkel et al. 2015) (see also Section I, Chapter 10, for methods to calculate X-ray spectra from X-ray tubes). The shape of the spectrum can be explained by the physical mechanisms that are responsible for the production of X-rays in the X-ray tube:

- Fast electrons can be diffracted and slowed down once they enter the anode surface. Due to the charged particles being decelerated (often multiple times), electromagnetic waves (in our case: X-rays) are radiated in a continuous range of energies. This phenomenon is known as *bremsstrahlung* and corresponds to the smooth part of the spectrum in Figure 34.2. The amount of deceleration is directly linked to the energy level of the emitted X-ray photon. If an electron directly collides into the nucleus of an anode atom, all the electron's energy is converted to X-ray radiation, a process that corresponds to the upper energy limit in the emitted spectrum (see Figure 34.2).
- X-rays can also be generated from a direct interaction of fast electrons with the inner shell electrons of the anode's surface. If an inner shell electron is kicked

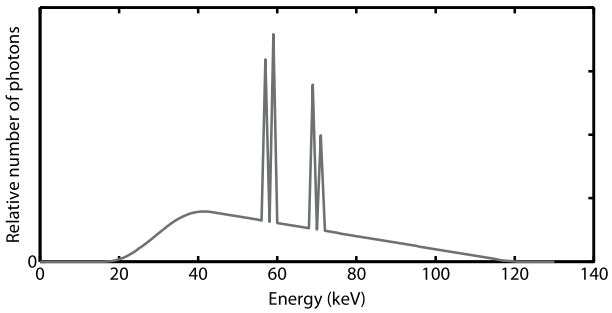

FIGURE 34.2 A typical representation of the X-ray spectrum in a biomedical CT scanner with an acceleration voltage of 120 keV.

out of the atom by a collision with a fast electron, an outer shell electron will take its place, a process that is accompanied by the emission of a photon. Since the binding energy difference between the same two shells is always constant, the emitted X-ray quanta resulting from this process can only have energy at a few discrete values. This creates sharp peaks in the emitted X-ray spectrum, known as *characteristic emission*.

The area on the anode that is hit by the fast electrons and from which the X-rays are emitted is called the *focal spot*. To obtain high resolution radiographs, a small focal spot size is desirable. The effect of the focal spot size is illustrated in Figure 34.3. In this figure, the *penumbra* is conceptually visualized, it is a blurry region at the edge of the scanned object's projection, which is due to partial absorption/illumination of the X-rays originating from the source with a larger spot size. Since only 1% of the kinetic energy of the fast electrons is converted into X-rays, while the remaining 99% goes into heat, the maximum heat capacity of the focal spot area is the major limiting factor for the focal spot size. If the heat delivered during a single exposure exceeds the focal spot heat capacity, the anode surface will melt. For this reason, a common technique is to continuously rotate the anode, thereby spreading the heat over a larger surface. Other, more advanced, techniques exist as well, such as the liquid metal jet anode, where a continuous flow of liquid metal replaces the solid anode (Hemberg et al. 2003).

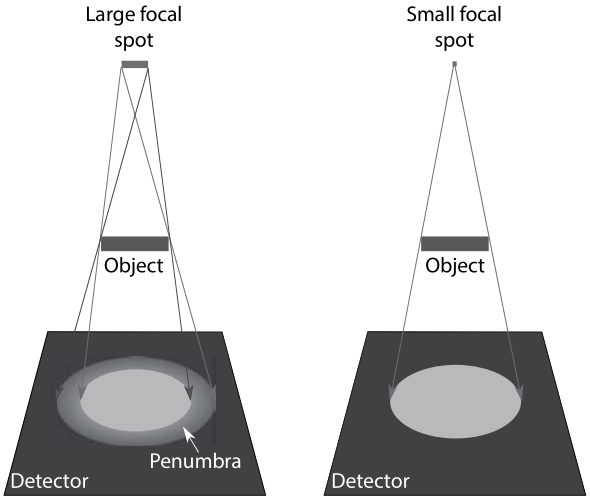

FIGURE 34.3 Illustration of the effect of a large focal spot size (left) in comparison to a small focal spot size (right).

In synchrotron facilities, X-rays are produced in a different manner (Winick 1995). The path of the high energy electrons that are contained within the storage ring is bent (corresponding to a radial acceleration), resulting in the production of X-rays. A major advantage in synchrotron facilities is that monochromatic X-ray beams (i.e., X-rays of a single energy level) can be produced at a high photon flux. To generate a proper photon flux in medical and lab-based CT systems, one has to work with polychromatic X-ray beams, consisting of photons within a continuous range of energies (see Figure 34.2).

In the remainder of this chapter, the intensity of an X-ray beam is denoted by $I(\eta, E)$, where η represents the distance traveled along the X-ray path, and E the energy bin. Often, a monochromatic X-ray beam is assumed, in which case the intensity is proportional to the number of photons and its intensity is denoted simply by $I(\eta)$. The X-ray beam intensity at the source position is denoted by $I(0) = I_0$.

34.2.1.2 X-ray Matter Interaction

As X-rays pass through an object, various scattering and absorption events result in a decreased intensity at the end of the object (Buzug 2008; Bushberg et al. 2011) (see also Section I, Chapter 1, for a general introduction to X-ray interactions in matter). This decreased intensity is described via the object's attenuation coefficient, μ, which models all physical mechanisms that lead to attenuation of the X-ray beam. The radiation intensity of a monochromatic beam after passing a distance, $\Delta\eta$, through a thin slice of homogeneous material with attenuation coefficient, μ, is described as follows:

$$I(\eta + \Delta\eta) = I(\eta) - \mu(\eta) I(\eta) \Delta\eta \tag{34.1}$$

$$= I(\eta)\,(1 - \mu(\eta)\Delta\eta) \tag{34.2}$$

These equations have two intuitively different interpretations. In Equation 34.1, one can observe that the difference in intensity after passing through the thin slice is proportional to the attenuation coefficient and the distance traveled through the slice. Another interpretation is given by Equation 34.2, where $(1 - \mu(\eta)\Delta\eta)$ can be seen as the probability of a single photon passing through the thin slice, and $I(\eta)\ (1 - \mu(\eta)\Delta\eta)$ as the expected number of photons that pass through the slice.

34.2.1.3 X-ray Detection

A crucial part of a CT system is the detection of the transmitted X-rays, thus the beam intensity, I, after it passed through the object. Various types of X-ray detection technologies are described in Buzug (2008). Conventional Xray detectors integrate the total number of photons in each detector pixel over a short period of time (the *exposure time*), without obtaining information about the energy of individual photons. An alternative is energy-resolved photon counting with dual energy detection (Kelcz et al. 1979) or multiple energy thresholds (Schlomka et al. 2008), providing the additional capability of counting individual photons, based on their detected energies.

Detectors can detect X-ray photons either directly or indirectly. Indirect-conversion detectors consist of two main components: (1) a light emitting material (scintillator) layer, which

converts the X-ray radiation into visible light photons; and (2) a photon detector that converts these light photons in an electric charge, which is, hence, proportional to the intensity of X-ray radiation. A typical example of such a detector is an amorphous silicon-based panel detector with a cesium iodide (CsI) scintillator deposed onto an array of photo-diodes. A second type of indirect-conversion detectors use a photon detector that consists of charge-coupled devices (CCDs). These CCD-based detectors use fiber optics to guide the light from the scintillator to the CCD camera.

Direct-conversion detectors have no intermediate stage in which visible light photons are generated, but directly convert X-ray photons into electric charge. Such detectors consist of a semi-conductor layer such as silicon (Si) or gallium arsenide (GaAS) to which an offset voltage is applied. X-ray photons entering the semi-conductor layer generate electron-hole pairs. The charges are accumulated and read using a thin-film transistor (TFT) array. Direct-conversion detectors are much more efficient than indirect-conversion detectors.

34.2.2 The Law of Beer–Lambert

The law of Beer–Lambert is an important law that is often exploited in the theory of computed tomography. It relates the attenuation of light (in our case X-rays) to the properties of the material through which the light is propagating. The Beer–Lambert law states that a monochromatic X-ray with radiation intensity, I_0, that propagates a distance, s, through a material with position dependent attenuation coefficient, $\mu(\eta)$, has a remaining intensity given by

$$I(s) = I_0 e^{-\int_0^s \mu(\eta)d\eta} \tag{34.3}$$

The law is conceptually visualized in Figure 34.4.

The law of Beer–Lambert can be derived as follows. Let η be the axis parallel to the direction of the X-ray beam (see Figure 34.4). Rearranging the terms in Equation 34.1 gives

$$\frac{I(\eta + \Delta\eta) - I(\eta)}{\Delta\eta} = -\mu(\eta)I(\eta) \tag{34.4}$$

which results in

$$\frac{dI}{d\eta}(\eta) = -\mu(\eta)I(\eta) \tag{34.5}$$

after taking the limit for $\Delta\eta \to 0$. Equation 34.5 is an ordinary linear differential equation which can be solved by rearranging the terms and multiplying the equation with the integrating factor, $e^{\int_0^\eta \mu(\eta')d\eta'}$, leading to

$$\frac{dI}{d\eta}(\eta)e^{\int_0^\eta \mu(\eta')d\eta'} + \mu(\eta)I(\eta)e^{\int_0^\eta \mu(\eta')d\eta'} = 0 \tag{34.6}$$

Applying the product rule backward, this simplifies to

$$\frac{d}{d\eta}\left(I(\eta)e^{\int_0^\eta \mu(\eta')d\eta'}\right) = 0 \tag{34.7}$$

Integrating both sides of this equation, leads to

$$\int_0^s \frac{d}{d\eta}\left(I(\eta)e^{\int_0^\eta \mu(\eta')d\eta'}\right)d\eta = \int_0^s 0\,d\eta \tag{34.8}$$

$$\Leftrightarrow \quad I(s)e^{\int_0^s \mu(\eta')d\eta'} - I(0)e^{\int_0^s \mu(\eta')d\eta'} = 0 \tag{34.9}$$

$$\Leftrightarrow \quad I(s)e^{\int_0^s \mu(\eta')d\eta'} = I(0) \tag{34.10}$$

$$\Leftrightarrow \quad I(s) = I(0)e^{-\int_0^s \mu(\eta')d\eta'} \tag{34.11}$$

This completes the derivation, since Equation 34.11 is equivalent to Equation 34.3.

The law of Beer–Lambert is particularly of interest, because it can be transformed to a linear relation between the measured data and the attenuation coefficients of the object. That is, Equation 34.3 can be rewritten as

$$-\ln\left(\frac{I(s)}{I_0}\right) = \int_0^s \mu(\eta)d\eta \tag{34.12}$$

If the incoming beam intensity, I_0, is known, which is almost always the case in practical applications, the left hand side of Equation 34.12 is fully known. The process of dividing the measured intensity by the incoming beam intensity, I_0, is known as *flat-field correction*. In the remainder of this chapter, it is assumed that the available projection data is always in its preprocessed form, $-\ln(I(s)/I_0)$.

34.2.3 Projection Geometries

A projection geometry refers to the setup and position of detector and source. Without intending to cover a full oversight of all possible projection geometries, some common projection geometries are described here.

In the 2D case, a *parallel beam* geometry and *fan beam* geometry are the most common. In the parallel beam geometry, all rays in a single projection are parallel to each other, as is visualized in Figure 34.5a. In fan beam geometry, all rays start from a single point source and reach the detector in equidistantly spaced detector points (see Figure 34.5b). In 3D, the parallel beam (see Figure 34.5c) and *cone* beam (see Figure 34.5d) are the 3D analog of the

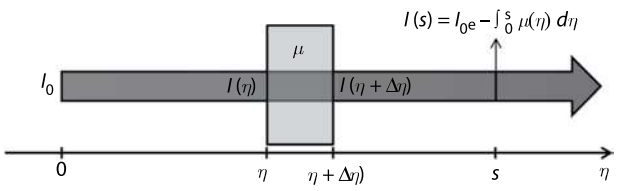

FIGURE 34.4 Illustration of the Beer–Lambert law.

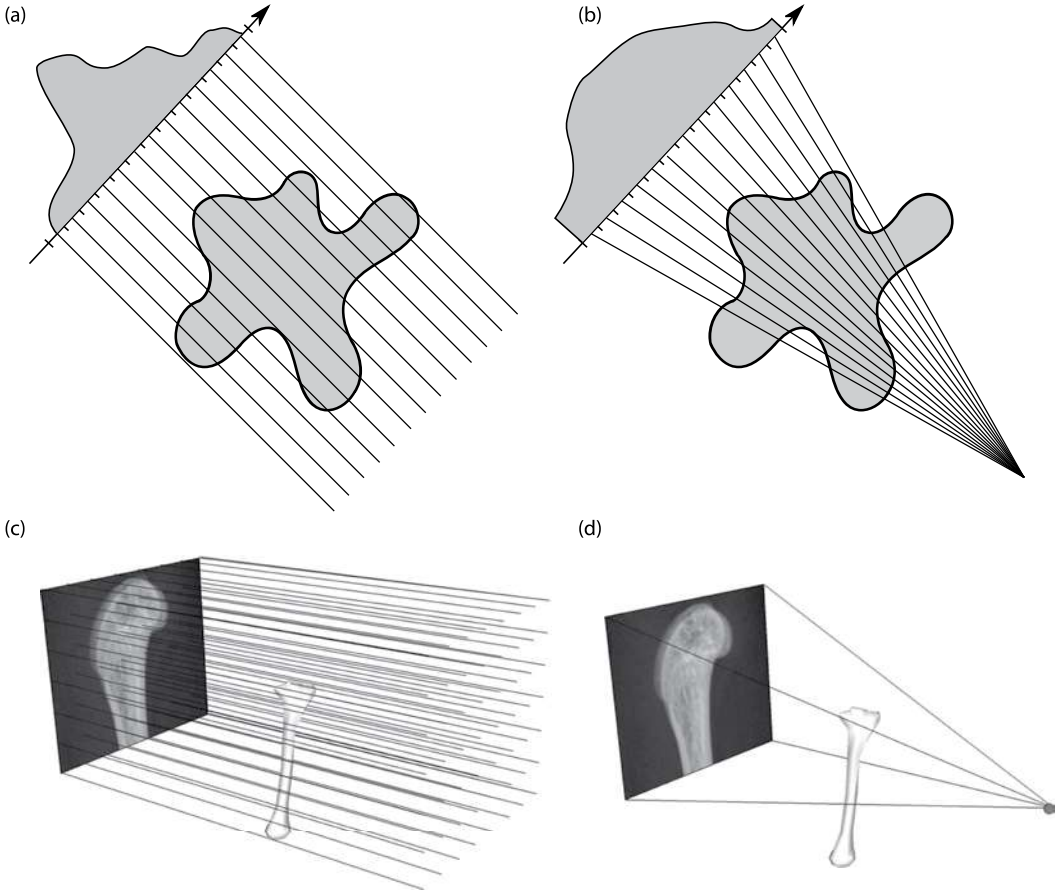

FIGURE 34.5 Illustration of different projection geometries for the 2D and 3D case. (a) 2D parallel beam, (b) 2D fan beam, (c) 3D parallel beam, (d) 3D cone beam.

2D parallel beam and fan beam geometry, respectively. If cone beam projections are acquired in a circular trajectory, the term *circular* cone beam geometry is utilized. A *helical* cone beam geometry refers to cone beam projections that are acquired in a helical trajectory (a geometry that is quite common in medical CT).

34.3 Reconstruction Methods

X-ray radiography is the most widespread medical imaging method, but it suffers from major drawbacks: (1) There is no depth information in the radiographic images; (2) X-ray radiographs often lack image contrast. That is, large changes in attenuation coefficient may result in only small changes in image intensity. The solution to these drawbacks is CT. In CT, the 3D attenuation distribution of the object that was imaged is reconstructed from a set of X-ray radiographs (projection data) that were acquired from different angular viewpoints.

The goal of CT reconstruction is to find the distribution of attenuation coefficients within the scanned object, based on the measured projection data (see Figure 34.1b). In what follows, different types of reconstruction methods are described. These can be roughly sub-divided into three classes. *Analytical reconstruction methods* (Section 34.3.1) model the object's attenuation coefficients as a function of its spatial coordinates and exploit various analytical properties of the forward projection model in order to generate a reconstruction. In *algebraic reconstruction methods* (Section 34.3.2), the object is modeled on a discrete pixel/voxel grid, and the reconstruction problem is reduced to a large system of linear equations. In a final class of methods, *statistical reconstruction methods* (Section 34.3.3), various statistical properties of the acquisition process are exploited, and typically some likelihood function, incorporating these statistical properties, is optimized.

In what follows, all methods are described for the 2D case, such as a 2D object from which one-dimensional projections are acquired. For algebraic and statistical methods, the extension to the 3D case is straightforward, but will not be described here.

34.3.1 Analytical Reconstruction Methods

In the analytical approach, the object's attenuation coefficients are described as a function, $f: \mathbb{R} \times \mathbb{R} \rightarrow \mathbb{R}$ that maps the spatial coordinate (x, y) to its corresponding local attenuation coefficient, μ. In Sections 34.3.1.1 and 34.3.1.2, the Radon transform and the Fourier slice theorem are introduced. The latter makes a remarkable connection between the analytical projections and the two-dimensional Fourier transform of $f(x, y)$. These concepts lead to the Filtered Back projection (FBP) reconstruction algorithm in Section 34.3.1.3. Finally, some other analytical reconstruction methods are discussed in Section 34.3.1.4 (see also Section III, Chapter 33, for a general description of analytical reconstruction methods in CT).

34.3.1.1 Radon Transform

The projection process in tomography consists of straight rays traversing the object, f, at a certain angle and a certain distance from the center of the detector to the ray (this is illustrated in the left part of Figure 34.6). A particular line, $L(r, \theta)$, at a counterclockwise angle, θ, from the y-axis and at a signed distance, r, from the origin is defined as follows:

$$L(r,\theta) = \{(x,y) \in \mathbb{R}^2 \big| x\cos\theta + y\sin\theta = r\} \tag{34.13}$$

Remember that the log- and flat-field-corrected projections are theoretically given by a line integral of the attenuation coefficients (see Equation 34.12). Therefore, a particular projection value, $p_\theta(r)$, is defined as the line integral through $f(x, y)$ over the line $L(r, \theta)$:

$$p_\theta(r) = \int_{L(r,\theta)} f(x,y)\,ds \tag{34.14}$$

The Radon transform, $\mathcal{R}$, is the transformation that maps the object function, $f(x, y)$, to the complete set of projection values, thus:

$$f(x,y) \overset{\mathcal{R}}{\leftrightarrow} \{p_\theta(r) | \theta \in [0,\pi[, r \in \mathbb{R}\} \tag{34.15}$$

Equation 34.15 implies that $(\mathcal{R}f)(\theta, r) = p_\theta(r)$

34.3.1.2 Fourier Slice Theorem

The Fourier slice theorem for two dimensions is conceptually visualized in Figure 34.6. The theorem states that the one-dimensional Fourier transform of a parallel beam projection of $f(x, y)$ at a certain angle is exactly the same as the slice through the Fourier transform, $F(u, v)$, which is perpendicular to the projection direction. The Fourier slice theorem is stated more precisely in the following theorem:

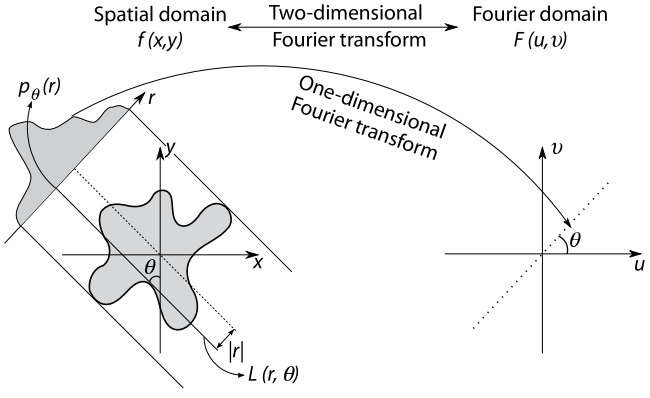

FIGURE 34.6 Schematic overview of the analytical projection model and the Fourier slice theorem. The one-dimensional Fourier transform of the projection data at angle θ yields a slice through the Fourier domain, which is perpendicular to the projection direction.

Theorem. Let f: $\mathbb{R} \times \mathbb{R} \to \mathbb{R}$: $(x,y) \mapsto f(x,y)$ be a two-dimensional function and define its projection $p_\theta(r)$: $\mathbb{R} \to \mathbb{R}$: $r \mapsto p_\theta(r)$ as in Equation 34.14. Denote the two-dimensional Fourier transform of $f(x, y)$ as $F(u, v)$ and the one-dimensional Fourier transform of $p_\theta(r)$ as $P_\theta(q)$. Then the following equality holds:

$$F(u,v)\Big|_{\substack{u=q\cos(\theta)\\ v=q\sin(\theta)}} = P_\theta(q) \tag{34.16}$$

Proof: The proof of the Fourier slice theorem is straightforward for $\theta = 0$, which can be assumed without loss of generality. Indeed, if the theorem applies for $\theta = 0$, then the theorem is also valid for any $\theta \neq 0$, since a rotation in the spatial domain corresponds to exactly the same rotation in Fourier space. It is, hence, sufficient to prove that $F(q, 0) = P_0(q)$.

The line integral, $p_0(r)$, corresponds to

$$p_0(r) = \int_{L(r,0)} f(x,y)\,ds = \int_{-\infty}^{\infty} f(r,y)\,dy \tag{34.17}$$

since $L(r, 0)$ is the line $x = r$. The Fourier transform of $f(x, y)$ is

$$F(u,v) = \int_{-\infty}^{\infty}\int_{-\infty}^{\infty} f(x,y)e^{-2\pi i(xu+yv)}dx\,dy \tag{34.18}$$

Evaluated in $u = q$ and $v = 0$, Equation 34.18 becomes

$$F(q,0) = \int_{-\infty}^{\infty}\int_{-\infty}^{\infty} f(x,y)e^{-2\pi ixq}dx\,dy \tag{34.19}$$

$$= \int_{-\infty}^{\infty}\left[\int_{-\infty}^{\infty} f(x,y)dy\right]e^{-2\pi ixq}\,dx \tag{34.20}$$

$$= \int_{-\infty}^{\infty} p_0(x)e^{-2\pi ixq}dx \tag{34.21}$$

$$= P_0(q) \tag{34.22}$$

which concludes the proof.

Note that, if enough projections, $p_\theta(r)$, can be acquired, the Fourier domain of the object can be fully sampled. A simple inverse Fourier transform could, hence, suffice to reconstruct the object function, $f(x, y)$. In practice, however, projections are given in a finite number of detector pixels, and can only be acquired at a finite number of angles. Assuming a parallel beam projection geometry, the Fourier space of the object, $f(x, y)$, is radially sampled, as is illustrated in Figure 34.7. To use the fast Fourier transform (FFT) algorithm (Heideman et al. 1984) to perform

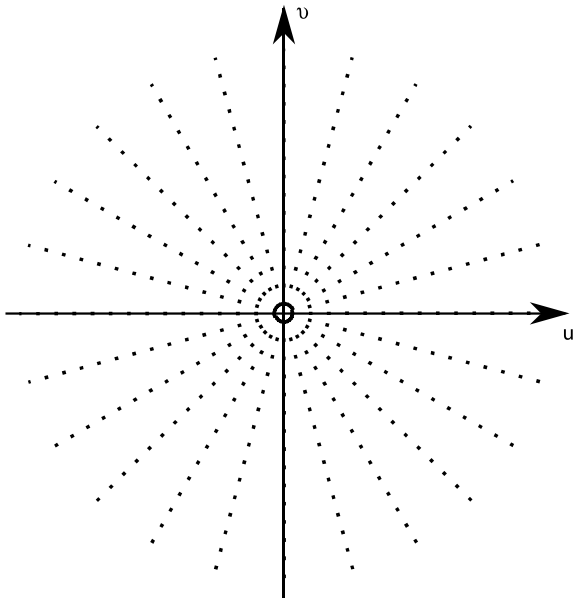

FIGURE 34.7 Parallel beam projections yield a radial filling of values in the Fourier space.

the inverse Fourier transform in an actual implementation, the radially sampled Fourier space must be resampled on a regular grid. Therefore, interpolation is necessary. However, this introduces large interpolation errors in the higher frequency part of the spectrum, since samples are only sparsely available in this region. These high spatial frequencies correspond to fine details in the object function, and, since they are less accurately represented after the resampling, image quality is seriously degraded. In the next section, an analytical method that compensates for the fact that points in Fourier space are more densely sampled near the origin, is introduced.

34.3.1.3 Filtered Back Projection (FBP)

The Filtered Back Projection (FBP) reconstruction method is based on the following analytical formula:

$$f(x,y) = \int_0^{\pi} \left\{ \int_{-\infty}^{\infty} P_\theta(q)|q| e^{2\pi i q(x\cos\theta + y\sin\theta)}\, dq \right\} d\theta \quad (34.23)$$

Before proving this formula, its different components are explained. As can be observed from Equation 34.23, the FBP formula gives rise to a simple two step approach for calculating a reconstruction of the scanned object, based on the measured projection data:

1. Filter the projection data, $p_\theta(r)$, by multiplying its Fourier transform, $P_\theta(q)$, with $|q|$ and calculating the inverse Fourier transform. This step corresponds to the inner integral in Equation 34.23.
2. For a particular location in the image domain, (x, y), sum up all the filtered projection data that corresponds to the lines $x\cos\theta + y\sin\theta$ with $\theta \in [0, \pi]$. This step corresponds to the outer integral in Equation 34.23.

This approach can be turned into a practical algorithm, keeping the following in mind:

- Since projection data is acquired at a finite number of detector pixels, and, thus, only available at discrete locations, the Fourier and inverse Fourier transform are performed with the FFT algorithm. Also, the formula is only evaluated at discrete locations in the spatial domain, typically on the pixel coordinates of a pixel grid. Therefore, in a practical implementation, the entire formula in Equation 34.23 is discretized by changing the integrals to sums.
- Projection data needs to be acquired over the full angular range, $[0, \pi]$, corresponding to the outer integral in Equation 34.23. Also, the scanned object must be fully inside the field of view, so that $p_\theta(r)$ and, hence, also $P_\theta(q)$ is available on its entire domain, thereby ensuring that the inner integral in Equation 34.23 can be calculated. If these assumptions are violated, the reconstructed image will contain artifacts.
- In a practical implementation, the FBP formula in Equation 34.23 is never evaluated individually at different locations in the spatial domain. Typically, the FBP formula is evaluated simultaneously at all pixel coordinates by first filtering the projection data with the high-pass filter $|q|$ (in Fourier space) and subsequently summing all back-projections of each projection onto the pixel grid. A back-projection simply places the values of the projection, $p_\theta(r)$ (with r describing the signed distances to all rays in a single projection defined by the fixed angle θ) at all pixels that coincide with the line $x\cos\theta + y\sin\theta = r$. This implies that the FBP algorithm as described here is only suitable for a parallel beam geometry.

The application of the high-pass filter, $|q|$, compensates for the high density sampling ratio in the low frequency domain and the low density sampling ratio in the high frequency domain (see Figure 34.7). In the context of FBP, the high-pass filter, $|q|$, is usually referred to as the "ramp" filter, because of its shape in the Fourier domain.

The FBP formula can be derived as follows. First, the rectangular coordinate system (u, v) over which it is integrated in the inverse Fourier transform formula, such as

$$f(x,y) = \int_{-\infty}^{\infty}\int_{-\infty}^{\infty} F(u,v) e^{2\pi i(xu+yv)}\, du\, dv \quad (34.24)$$

is changed to a polar coordinate system (q, θ). This is achieved by making the substitution $u = q\cos\theta$ and $v = q\sin\theta$, which results in

$$du\,dv = \begin{vmatrix} \cos\theta & -q\sin\theta \\ \sin\theta & q\cos\theta \end{vmatrix} dq\,d\theta = q\,dq\,d\theta \quad (34.25)$$

The inverse Fourier transform in Equation 34.24 can now be expressed in polar form as

$$f(x,y) = \int_0^{2\pi}\int_0^{\infty} F(q\cos\theta, q\sin\theta) e^{2\pi i q(x\cos\theta + y\sin\theta)} q\, dq\, d\theta \quad (34.26)$$

The integral in Equation 34.26 can be split into two parts by integrating θ from 0 to π and from π to 2π and further rewritten as follows:

$$\begin{aligned} f(x,y) &= \int_0^{\pi}\int_0^{\infty} F(q\cos\theta, q\sin\theta)e^{2\pi iq(x\cos\theta+y\sin\theta)}q\,dq\,d\theta \\ &+ \underbrace{\int_0^{\pi}\int_0^{\infty} F(q\cos(\theta+\pi), q\sin(\theta+\pi))\, e^{2\pi iq(x\cos(\theta+\pi)+y\sin(\theta+\pi))}q\,dq\,d\theta}_{=\int_0^{\pi}\int_0^{\infty} F(-q\cos\theta,-q\sin\theta)e^{2\pi i(-q)(x\cos\theta+y\sin\theta)}q\,dq\,d\theta} \\ &\quad =\int_0^{\pi}\int_{-\infty}^{0} F(q\cos\theta,q\sin\theta)e^{2\pi iq(x\cos\theta+y\sin\theta)}(-q)\,dq\,d\theta \\ &= \int_0^{\pi}\int_{-\infty}^{\infty} F(q\cos\theta,q\sin\theta)\,|q|\,e^{2\pi iq(x\cos\theta+y\sin\theta)}\,dq\,d\theta \end{aligned} \tag{34.27}$$

Substituting the Fourier slice theorem formula (see Equation 34.16) into Equation 34.27 leads to

$$f(x,y) = \int_0^{\pi}\int_{-\infty}^{\infty} P_{\theta}(q)\mid q\mid e^{2\pi iq(x\cos\theta+y\sin\theta)}dq\,d\theta \tag{34.28}$$

which completes the derivation of the FBP formula in Equation 34.23.

34.3.1.4 Other Analytical Reconstruction Methods

Various variants on the FBP algorithm have been proposed in the literature. Most variants focus on redesigning the ramp filter, $|q|$, in Equation 34.23. One approach is to train a neural network that learns an optimal filter for a certain class of objects (Pelt and Batenburg. 2013). Another approach consists of approximating algebraic methods (see Section 34.3.2) by selecting a proper FBP filter (Batenburg and Plantagie 2012). The FBP algorithm described in Section 34.3.1.3 is suitable for a 2D parallel beam geometry. For fan beam, another formula and approach must be followed (Kak and Slaney 2001). For the 3D case, the Feldkamp (FDK) algorithm is a common choice for reconstructing from circular cone beam projections (Feldkamp et al. 1984). For helical cone beam CT, other algorithms are available (Kudo et al. 2004).

34.3.2 Algebraic Reconstruction Methods

In the algebraic approach, the object's attenuation coefficients are modeled by a discrete representation of the object function, $f(x, y)$, typically on a pixel grid. The discretization process is presented in Section 34.3.2.1. A well-known algebraic reconstruction method, the simultaneous iterative reconstruction technique (SIRT), is derived in Section 34.3.2.2, after which other algebraic reconstruction methods such as algebraic reconstruction technique (ART) and simultaneous algebraic reconstruction technique (SART) are discussed. All mentioned algebraic reconstruction methods can be easily implemented with the open source ASTRA toolbox (van Aarle et al. 2015, 2016).

34.3.2.1 Discretization

A typical approach is to represent the scanned object on a pixel (or, in the 3D case, voxel) grid. This is conceptually visualized in Figure 34.8, which is the discrete analog of the left part of Figure 34.6. In the discretization on a pixel grid, it is assumed that the object has a constant attenuation value within each pixel. Assuming the pixel grid consists of N pixels, the object function, $f(x, y)$, is approximated as $f(x,y) \approx \sum_{j=1}^{N} x_j\phi_j$, with ϕ_j the pixel basis function for the jth pixel, the constant attenuation value which is zero outside the pixel and one inside, and x_j within the jth pixel. The basis functions, ϕ_j, do not necessarily need to be pixel basis functions. Other choices are possible as well, such as generalized Kaiser-Bessel functions (a.k.a. blobs) (Matej and Lewitt 1992). Since the object is modeled by a finite number of attenuation values, it can be represented as a column vector, $x = (x_j) \in \mathbb{R}^N$.

In practice, the measured projection data is also discrete: it consists of a finite number of measured projection values, each one corresponding to a specific detector pixel at a specific angle. Let M denote the total number of measured projection values for all angles, which are log-corrected and ordered in a vector $p = (p_i) \in \mathbb{R}^M$. Denote θ_i as the counter-clockwise angle from the y-axis and r_i as the signed distance from the origin to the center of the detector pixel corresponding to p_i. Following Equation 34.14, each projection value, p_i, can be modeled as

$$p_i = \int_{-\frac{\Delta r}{2}}^{\frac{\Delta r}{2}} p_{\theta_i}(r_i + r')dr' = \int_{-\frac{\Delta r}{2}}^{\frac{\Delta r}{2}}\int_{L(r_i,\theta_i)} f(x,y)ds\,dr' \tag{34.29}$$

where Δr represents the detector pixel width. In algebraic reconstruction methods, the forward projection model of Equation 34.29 is approximated by $p_i \approx \sum_{j=1}^{N} w_{ij}x_j$, where w_{ij} represents

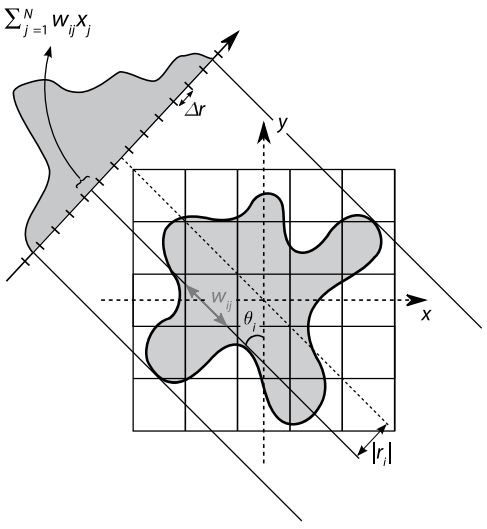

FIGURE 34.8 Illustration of the discrete representation of the object and the projection. In this image, the contribution, w_{ij}, of pixel j to the projection value with index i is represented as the ray-intersection length of projection line i with pixel j.

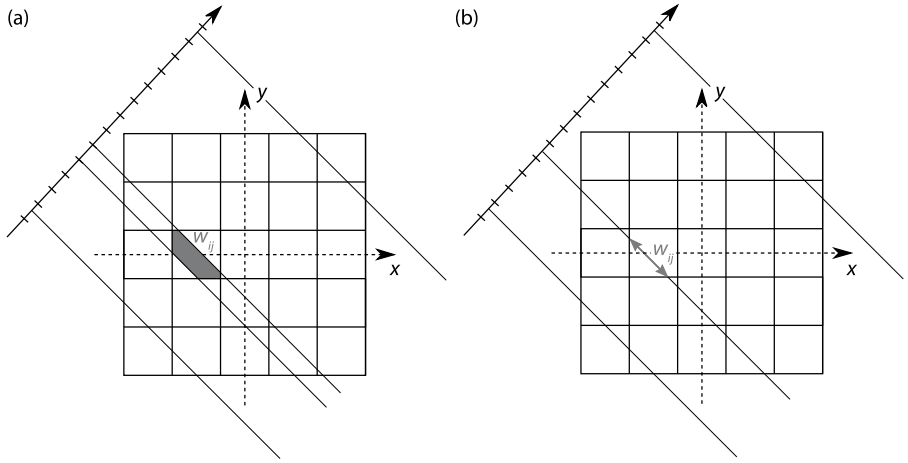

FIGURE 34.9 Illustration of two different approaches to calculate the weights of the forward projection matrix $\boldsymbol{W}$. (a) Strip-kernel, (b) line-kernel.

the contribution of pixel j to the projection value with index i. This is also illustrated in Figure 34.8. The complete projection data, p, can then be simulated by $\boldsymbol{Wx}$, where $\boldsymbol{W} = (w_{ij}) \in \mathbb{R}^{M\times N}$ is a sparse matrix that collects all weights, w_{ij}. The weights can be calculated in a variety of ways. The most precise calculation involves a strip-kernel, which is visualized in Figure 34.9a, where the weight w_{ij} is equal to the fractional area of the jth pixel intercepted by the ith ray. A computationally faster approximation is given by the line-kernel, where the weight w_{ij} equals the ray-intersection length of the ith ray with the jth pixel (see Figure 34.9b), or by a linear-kernel (Joseph 1982) (also known as Joseph's method), where the contribution of the ray to the projection value is determined by linearly interpolating between the two nearest pixels of the intersection of the ray and the row or column.

Directly solving the system of linear equations, $\boldsymbol{Wx} = \boldsymbol{p}$, for an exact solution $\boldsymbol{x}$ is typically infeasible, since noise and discretization effects render the system of linear equations inconsistent. Therefore, algebraic methods typically minimize the projection distance $\|\boldsymbol{Wx} - \boldsymbol{p}\|$ for some norm $\|\cdot\|$.

The projection data acquired from a 2D object is usually represented as a *sinogram*. A sinogram collects the projections from a 2D object in a matrix, where columns typically represent the different detector pixels and the rows the different projection angles. An example of a sinogram acquired from the Shepp–Logan phantom (Shepp and Logan 1974) is given in Figure 34.10.

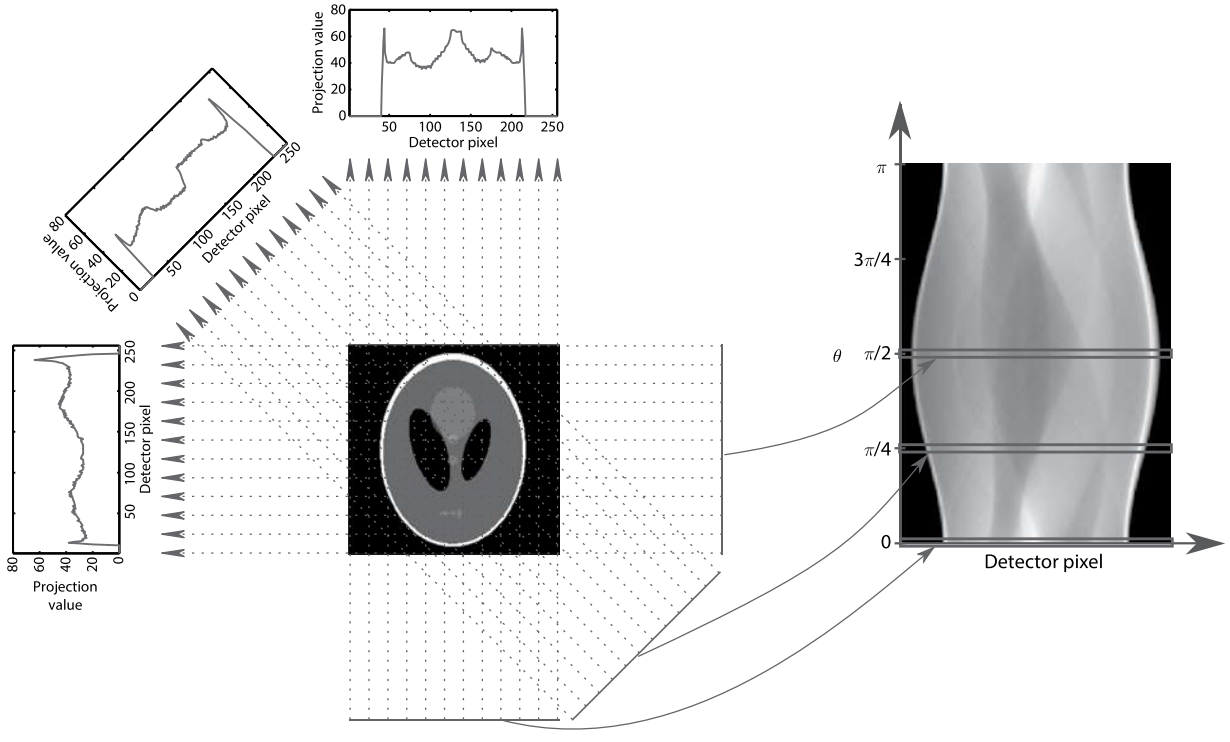

FIGURE 34.10 An example of a sinogram acquired with a parallel beam geometry from the Shepp–Logan phantom. The projections acquired at $\theta = 0$, $\theta = \pi/4$, and $\theta = \pi/2$ are explicitly shown, and their connection with the sinogram is illustrated.

34.3.2.2 Simultaneous Iterative Reconstruction Technique (SIRT)

The simultaneous iterative reconstruction technique (SIRT) is an algebraic reconstruction algorithm known to converge to a solution of

$$x^* = \arg\min_x \left(\|W_x - \boldsymbol{p}\|_{\boldsymbol{R}}^2 \right) \tag{34.30}$$

where $\boldsymbol{R} = (r_{ij}) \in \mathbb{R}^{M \times M}$ is the diagonal matrix with inverse row sums of the projection matrix $\boldsymbol{W}$ (its diagonal elements are given by $r_{ii} = 1/\Sigma_j w_{ij}$) and $\|\boldsymbol{Wx} - \boldsymbol{p}\|_{\boldsymbol{R}}^2 = (\boldsymbol{Wx} - \boldsymbol{p})^T \boldsymbol{R}(\boldsymbol{Wx} - \boldsymbol{p})$ (Jiang and Wang 2003; Buzug 2008; Gregor and Benson 2008). Starting from an initial reconstruction, $\boldsymbol{x}^{(0)} = \boldsymbol{0}$, the SIRT algorithm iteratively updates the reconstruction as follows:

$$\boldsymbol{x}^{(k+1)} = \boldsymbol{x}^{(k)} + \boldsymbol{CW}^T \boldsymbol{R}(\boldsymbol{p} - \boldsymbol{Wx}^{(k)}) \tag{34.31}$$

where $\boldsymbol{C} = (c_{ij}) \in \mathbb{R}^{N \times N}$ is defined as the diagonal matrix with the inverse column sums of $\boldsymbol{W}$ (i.e., $c_{jj} = 1/\Sigma_j w_{ij}$). Before demonstrating the connection between Equations 34.30 and 34.31, the iterative update in Equation 34.31 is analyzed more closely. The update in Equation 34.31 is illustrated in Figure 34.11, and consists of the following steps:

1. Starting from the current estimate, $\boldsymbol{x}^{(k)}$, a forward projection, $\boldsymbol{Wx}^{(k)}$, is simulated.
2. The *projection difference* $\boldsymbol{p} - \boldsymbol{Wx}^{(k)}$ is calculated. This difference indicates where and how much the simulated projection data, $\boldsymbol{Wx}^{(k)}$, is different from the measured projection data, $\boldsymbol{p}$. It quantifies the reconstruction quality of the current estimate, $\boldsymbol{x}^{(k)}$.
3. The projection difference, $\boldsymbol{p} - \boldsymbol{Wx}^{(k)}$, is weighted with the inverse row sum matrix, $\boldsymbol{R}$. Intuitively, projection value differences corresponding to rays with a long intersection length with the pixel grid of the reconstruction domain get a small weight and projection value differences corresponding to rays that intersect only shortly with the reconstruction domain get a large weight. A large weight (and, hence, short ray-intersection length) indicates that the projection difference in the particular detector pixel has a large influence in the update. This makes sense, since that ray intersects with only a few pixels in the reconstruction domain, and thus the projection difference in the corresponding detector pixel is a good indication for how to update the pixels on that particular ray. If a ray intersects a lot of pixels, the projection difference is less trustworthy, since the projection value is based on the (weighted) sum of lots of attenuation values along the ray.
4. The back-projected weighted projection difference, $\boldsymbol{W}^T \boldsymbol{R}(\boldsymbol{p} - \boldsymbol{Wx}^{(k)})$ is calculated. That is, all projection differences are "smeared back" over the reconstruction domain by simply assigning the projection difference value of each ray to all pixels along that ray, weighted with the ray-pixel-intersection length.
5. The result is weighted with the inverse column sum matrix, $\boldsymbol{C}$. For a particular pixel, this corresponds to dividing the pixel value of the update by the combined length of all rays that intersected that pixel. The resulting update reflects how the reconstruction should be updated in order to reduce the projection difference.
6. The update is added to the current reconstruction, and the algorithm continues from the first step until a certain stopping criterion is reached. The stopping criterion can consist of stopping the algorithm after a pre-defined number of iterations or after the projection distance has reached a certain threshold value.

The connection between Equations 34.30 and 34.31 can be made as follows. The normal equations for Equation 34.30 are given by

$$\boldsymbol{W}^T \boldsymbol{RWx} = \boldsymbol{W}^T \boldsymbol{Rp} \tag{34.32}$$

Pre-conditioning Equation 34.32 with $\boldsymbol{C}$ and rewriting the equations gives

$$\boldsymbol{CW}^T \boldsymbol{RW}x = \boldsymbol{CW}^T \boldsymbol{Rp} \tag{34.33}$$

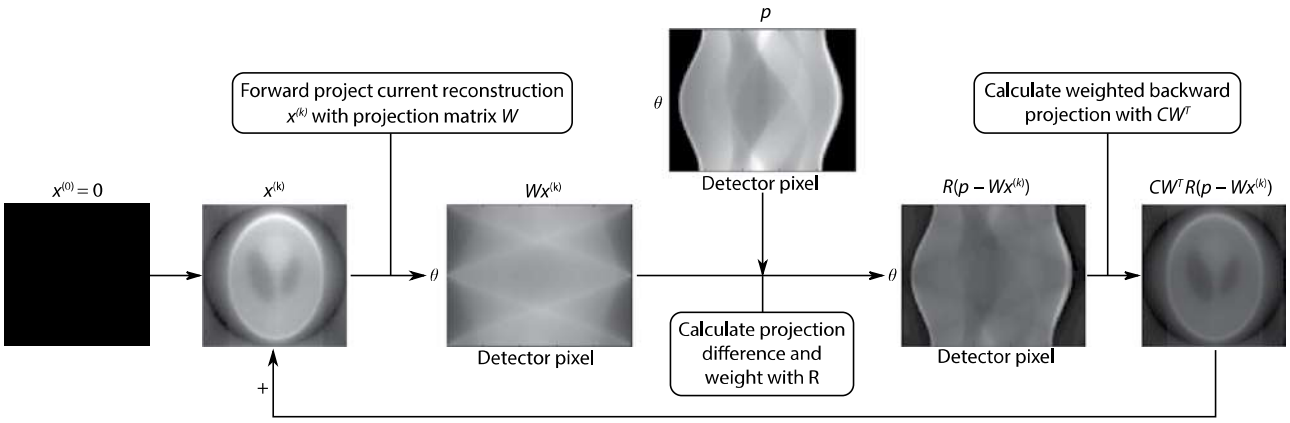

FIGURE 34.11 The SIRT update process illustrated with the Shepp–Logan phantom.

sense that artifacts can be reduced, or high quality reconstructions can be reconstructed from only a few projections. Some examples:

- If the object consists of only a few discrete grey levels, the discrete algebraic reconstruction technique (DART) has shown great potential for practical applications (Batenburg and Sijbers 2011; Dabravolski et al. 2014). In fact, an entire domain, named "discrete tomography", deals with the reconstructions of such objects (Herman and Kuba 2008).
- Often, a segmentation of the reconstruction is of interest. Various algorithms combine the segmentation and the reconstruction step into one algorithm, thereby simultaneously improving both steps (van Aarle et al. 2011; Roelandts et al. 2012).
- Specific algorithms have been developed in medical imaging for reducing metal artifacts, such as the normalized metal artifact reduction (NMAR) (Meyer et al. 2010) and the frequency split metal artifact reduction (FSMAR) (Meyer et al. 2012) algorithms.
- In region of interest (ROI) tomography, the goal is to reconstruct only a small region inside the object. Often, certain assumptions are made about the region of the object surrounding the ROI, thereby greatly improving image quality (Hsung and Lun 2000; Anoop and Rajgopal 2009; Sidky et al. 2014).
- Another approach consists of changing the acquisition protocol from a step-and-shoot approach (i.e., stopping the gantry at each acquisition angle to acquire a projection) to a continuous gantry rotation. This can be modeled in the reconstruction algorithm, resulting in algorithms which are particularly useful for ROI tomography (Cant et al. 2015).

34.3.3 Statistical Reconstruction Methods

In this section, a short introduction to statistical reconstruction methods is given. First, in Section 34.3.3.1, it is explained that the number of detected X-ray quanta follow a Poisson distribution. Next, in Section 34.3.3.2, the expectation maximization (EM) algorithm is derived. Finally, a class of more stable statistical algorithms is described in Section 34.3.3.3.

34.3.3.1 Poisson Distributed Noise

There are three components in X-ray imaging that can be modeled via statistical processes (the reader is referred to Buzug (2008) for more details):

- In a typical detector, X-ray photon detection is a statistically independent process. Therefore, the detection of multiple photons follows a Binomial distribution.
- The absorption of photons inside the object are also guided by Binomial statistics.
- The number of photons that leave the source follows a Poisson distribution.

Because Binomial selection of a Poisson process yields another Poisson process, the overall statistics can be modeled via a Poisson distribution:

$$P\left(I_i|I_i^*\right) = \frac{\left(I_i^*\right)^{I_i}}{I_i!}e^{-I_i^*} \quad i = 1,\ldots,M \tag{34.46}$$

where I_i denotes the number of measured X-ray quanta at the ith detector pixel, and I_i^* the expected number of detected X-ray quanta*. From Equation 34.46, it follows that

$$P(\boldsymbol{I}|\boldsymbol{I}^*) = \prod_{i=1}^{M}\frac{(I_i^*)^{I_i}}{I_i!}e^{-I_i^*} \tag{34.47}$$

where $\boldsymbol{I}$ and I_i^* are the column vectors collecting all the values I_i and I_i^* for all i, respectively.

34.3.3.2 Expectation Maximization (EM)

The underlying idea of the expectation maximization (EM) algorithm (Rockmore and Macovski 1977; Lange and Carson 1984; Lange et al. 1987) is to maximize the likelihood of acquiring the observed data while varying the expectation values of the attenuation coefficients of the scanned object. It can be derived as follows. Substituting the law of Beer–Lambert (i.e., the discrete version of Equation 34.3) into Equation 34.47 results in

$$L(\boldsymbol{x}^*) := P(\boldsymbol{I}|\boldsymbol{x}^*) = \prod_{i=1}^{M}\frac{\left(I_0e^{-\sum_{j=1}^{N}w_{ij}x_j^*}\right)^{I_i}}{I_i!}e^{-I_0e^{-\sum_{j=1}^{N}w_{ij}x_j^*}} \tag{34.48}$$

where $\boldsymbol{x}^*$ denotes the expected attenuation values for the scanned object. The product in the *likelihood* function, $L(\boldsymbol{x}^*)$, can be rewritten as a sum by taking its logarithm to produce the *log likelihood* function

$$l(\boldsymbol{x}^*) := \ln(L\ \boldsymbol{x}^*)) = \sum_{i=1}^{M}\left(I_i\ln(I_0) - I_i\sum_{j=1}^{N}w_{ij}x_j^* - \ln(I_i!) - I_0e^{-\sum_{i=1}^{N}w_{ij}x_j^*}\right) \tag{34.49}$$

Note that the maximization of Equations 34.49 or 34.48 yields the same result, since the logarithm is a monotonically increasing function. Therefore, maximizing $P(\boldsymbol{I}|\boldsymbol{x}^*)$ (which is the goal of the EM algorithm) is equivalent to solving the following optimization problem:

* This introduces a slight abuse of notation, since $\boldsymbol{I_0}$ was already defined in Section 34.2.1. $\boldsymbol{I_0}$ still denotes the radiation intensity at the source (in this case expressed in number of photons), whereas $\boldsymbol{I_i}$ ($\boldsymbol{i} = 1, \ldots, \boldsymbol{M}$) denotes the number of measured photons in the $\boldsymbol{i}$th detector pixel. Throughout this section, it is assumed that $\boldsymbol{I_0}$ is the same for all detector pixels. However, all derivations can be easily adapted to account for a detector pixel dependent $\boldsymbol{I_0}$ value.

$$\hat{\boldsymbol{x}}^* = \arg\max_{\boldsymbol{x}^* \geq \mathbf{0}} (l(\boldsymbol{x}^*)) \tag{34.50}$$

If the log likelihood function, $l(x^*)$, is concave, a global maximum is guaranteed. The concavity of $l(\boldsymbol{x}^*)$ can be shown by proving in the equivalent condition that the Hessian of $l(\boldsymbol{x}^*)$ is negative semi-definitive. The reader is referred to Lange and Carson (1984) for proof of this statement. Since a global maximum exists, the Karush–Kuhn–Tucker (KKT) conditions must be fulfilled. The inequality constraint in Equation 34.50 can be written in a more standard form for the KKT conditions, as $g_k(\boldsymbol{x}^*) := -x_k^* \leq 0$ for all $k = 1, \ldots, N$. The KKT conditions guarantee the existence of the KKT multipliers $\lambda_k \in \mathbb{R}$ ($k = 1, \ldots, N$), such that

$$(1) \quad \nabla l(\hat{\boldsymbol{x}}^*) - \sum_{k=1}^{N} \lambda_k \nabla g_k(\hat{\boldsymbol{x}}^*) = 0 \tag{34.51}$$

$$(2) \quad g_k(\hat{\boldsymbol{x}}^*) \leq 0 \quad \text{for all} \quad k = 1,\ldots,N \tag{34.52}$$

$$(3) \quad \lambda_k \geq 0 \quad \text{for all} \quad k = 1,\ldots,N \tag{34.53}$$

$$(4) \quad \lambda_k g_k(\hat{\boldsymbol{x}}^*) = 0 \quad \text{for all} \quad k = 1,\ldots,N \tag{34.54}$$

Conditions (1), (2), (3), and (4) are typically referred to as the stationarity condition, the primal feasibility condition, the dual feasibility condition, and the complementary slackness condition, respectively. The first condition (Equation 34.51) is equivalent to

$$\lambda_k = -\frac{\partial l}{\partial x_k^*}(\hat{\boldsymbol{x}}^*). \tag{34.55}$$

Substituting Equation 34.55 in the third and fourth conditions (Equations 34.53 and 34.54) yields

$$(3) \quad \frac{\partial l}{\partial x_k^*}(\hat{\boldsymbol{x}}^*) \leq 0 \tag{34.56}$$

$$(4) \quad \hat{x}_k^* \frac{\partial l}{\partial x_k^*}(\hat{\boldsymbol{x}}^*) = 0 \tag{34.57}$$

By calculating the partial derivative of l with respect to x_k^*, Equation 34.57 can be rewritten as

$$\hat{x}_k^* \frac{\partial l}{\partial x_k^*}(\hat{x}^*) = \hat{x}_k^* \left(I_0 \sum_{i=1}^{M} w_{ik} e^{-\sum_{j=1}^{N} w_{ij} \hat{x}_j^*} - \sum_{i=1}^{M} I_i w_{ik} \right) = 0 \tag{34.58}$$

$$\Leftrightarrow \quad \hat{x}_k^* I_0 \sum_{i=1}^{M} w_{ik} e^{-\sum_{j=1}^{N} w_{ij} \hat{x}_j^*} - \hat{x}_k^* \sum_{i=1}^{M} I_i w_{ik} = 0 \tag{34.59}$$

$$\Leftrightarrow \quad \hat{x}_k^* = \frac{\hat{x}_k^* I_0}{\sum_{i=1}^{M} I_i w_{ik}} \sum_{i=1}^{M} w_{ik} e^{-\sum_{j=1}^{N} w_{ij} \hat{x}_j^*} \tag{34.60}$$

In terms of the log-corrected projection data, $p_i = -\ln(I_i/I_0)$, Equation 34.60 can be rewritten as

$$\hat{x}_k^* = \hat{x}_k^* \frac{\sum_{j=1}^{N} w_{ik} e^{-\sum_{j=1}^{N} w_{ij} \hat{x}_j^*}}{\sum_{i=1}^{M} w_{ik} e^{-pi}} \tag{34.61}$$

From Equation 34.61, a fixed point iteration scheme can be derived. Starting from a non-zero reconstruction, $x^{(0)} = (x_k^{(0)})$, each individual pixel is updated as

$$x_k^{(n+1)} = x_k^{(n)} \frac{\sum_{j=1}^{M} w_{ik} e^{-\sum_{j=1}^{N} w_{ij} x_j^{(n)}}}{\sum_{i=1}^{M} w_{ik} e^{-pi}} k = 1,\ldots,N \tag{34.62}$$

The iterative algorithm in Equation 34.62 is the expectation maximization (EM) algorithm. In summary, the EM algorithm consists of the following steps:

1. Starting from the current estimate, $\boldsymbol{x}^{(n)}$, simulate the projection data with $e^{-\sum_{j=1}^{N} w_{ij} x_j^{(n)}}$ for $i = 1, \ldots, M$.
2. Back-project the simulated projection data. For the pixel with index k, this is achieved by processing all rays, and for each ray adding the corresponding simulated projection value multiplied with the intersection length of that particular ray with pixel k, thus

$$\sum_{i=1}^{M} w_{ik} e^{-\sum_{j=1}^{N} w_{ij} x_j^{(n)}} \tag{34.63}$$

3. Also, back-project the measured projection data, e^{-p_i} for $i = 1, \ldots, M$. In the kth pixel, this corresponds to

$$\sum_{i=1}^{M} w_{ik} e^{-p_i}. \tag{34.64}$$

4. Compare the back-projected simulated projection data to the back-projected measured projection data by calculating the ratio

$$\frac{\sum_{i=1}^{M} w_{ik} e^{-\sum_{j=1}^{N} w_{ij} x_j^{(n)}}}{\sum_{i=1}^{M} w_{ik} e^{-p_i}} \tag{34.65}$$

5. This ratio is multiplied in a pixel-by-pixel manner with the current reconstruction, $\boldsymbol{x}^{(n)}$, to produce an improved reconstruction, $\boldsymbol{x}^{(n+1)}$. The algorithm returns to step 1 and terminates based on some stopping criterion.

In practice, the EM algorithm of Equation 34.62 is rather unstable. Often some regularization term is added to the objective function in Equation 34.50, in order to improve the algorithm's stability. This is discussed in the following section.

34.3.3.3 Maximum A Posteriori (MAP) Reconstruction

In contrast to the EM algorithm, where the probability $P(\boldsymbol{I}|\boldsymbol{x}^*)$ is maximized, the posterior probability, $P(\boldsymbol{x}^*|\boldsymbol{I})$, is maximized with respect to $\boldsymbol{x}^*$ in the maximum *a posteriori* (MAP) approach (Lange and Fessler 1995). With Bayes' theorem, the posterior probability, $P(\boldsymbol{x}^*|\boldsymbol{I})$, can be written as a function of the conditional probability, $P(\boldsymbol{I}|\boldsymbol{x}^*)$:

$$P(\boldsymbol{x}^*|\boldsymbol{I}) = \frac{P(\boldsymbol{I}|\boldsymbol{x}^*)P(\boldsymbol{x}^*)}{P(\boldsymbol{I})} = P(\boldsymbol{x}^*)\prod_{i=1}^{M}\frac{P(I_i|\boldsymbol{x}^*)}{P(I_i)} \tag{34.66}$$

The product in Equation 34.66 can be transformed into a sum by taking the logarithm

$$\ln(P(\boldsymbol{x}^*|\boldsymbol{I})) = \ln(P(\boldsymbol{x}^*)) + \sum_{i=1}^{M}\{\ln(P(I_i|\boldsymbol{x}^*)) - \ln(P(I_i))\} \tag{34.67}$$

Maximization of Equation 34.67 over $\boldsymbol{x}^*$ is equivalent to minimizing $-\ln(P(\boldsymbol{x}^*|\boldsymbol{I}))$, such as

$$\hat{\boldsymbol{x}}^* = \arg\min_{\boldsymbol{x}^*\geq 0}\left(\sum_{i=1}^{M}\{-\ln(P(I_i|\boldsymbol{x}^*))\} - \ln(P(\boldsymbol{x}^*))\right), \tag{34.68}$$

where the irrelevant terms in the objective function were ignored. With the result in Equation 34.49 and by ignoring all irrelevant terms, the minimization problem in Equation 34.68 can be rewritten as

$$\hat{\boldsymbol{x}}^* = \arg\min_{\boldsymbol{x}^*\geq 0}\left(\sum_{i=1}^{M}\left(I_i\sum_{j=1}^{N}w_{ij}x_j^* + I_0e^{-\sum_{i=1}^{N}w_{ij}x_j^*}\right) - \ln(P(\boldsymbol{x}^*))\right) \tag{34.69}$$

A MAP reconstruction method solves the optimization problem in Equation 34.69. The term $-\ln(P(\boldsymbol{x}^*))$ typically represents the state of knowledge about the object $\boldsymbol{x}^*$. It is often referred to as the regularization term, $U(\boldsymbol{x}^*) = -\ln(P(\boldsymbol{x}^*))$. With this notation, the MAP optimization problem becomes

$$\hat{\boldsymbol{x}}^* = \arg\min_{\boldsymbol{x}^*\geq 0}\left(\sum_{i=1}^{M}\left(I_i\sum_{j=1}^{N}w_{ij}x_j^* + I_0e^{-\sum_{i=1}^{N}w_{ij}x_j^*}\right) + U(\boldsymbol{x}^*)\right) \tag{34.70}$$

A connection with the optimization problem in Equation 34.45 can be made as follows. First, rewrite Equation 34.70 by introducing $p_i^* = \sum_{j=1}^{N}w_{ij}x_j^*$:

$$\hat{\boldsymbol{x}}^* = \arg\min_{\boldsymbol{x}^*\geq 0}\left(\sum_{i=1}^{M}\left(I_ip_i^* + I_0e^{-p_i^*}\right) + U(\boldsymbol{x}^*)\right) \tag{34.71}$$

Next, calculate a second-order Taylor expansion of $I_ip_i^* + I_0e^{-p_i^*}$ around the log-corrected measured projection values, p_i, which results in (see Buzug (2008) for a detailed calculation):

$$\hat{\boldsymbol{x}}^* = \arg\min_{\boldsymbol{x}^*\geq 0}\left(\frac{1}{2}(p - W\boldsymbol{x}^*)^T D(p - W\boldsymbol{x}^*) + U(\boldsymbol{x}^*)\right) \tag{34.72}$$

with $D = \mathrm{diag}(I_1, I_2, \ldots, I_M)$. The only difference with Equation 34.45 is the weighting by the diagonal matrix, $\boldsymbol{D}$. Again, various choices can be made for the regularization term, $U(\boldsymbol{x}^*)$ (Chambolle 2004; Tang et al. 2009; Lou et al. 2010; Zhang et al. 2010). The optimization problem in Equations 34.72 and 34.70 can be optimized with a variety of algorithms (Lange and Fessler 1995; Tang et al. 2009). In general, algorithms based on the MAP principle are more stable than EM-like algorithms.

34.4 Dynamic Computed Tomography

In Sections 34.2 and 34.3, the classical tomography model was described, which assumes the scanned object to remain unaltered throughout the entire data acquisition process. This assumption is no longer valid in dynamic computed tomography, where projections are acquired from a time-varying object. Each projection, hence, corresponds to a different instance of the time-varying object, as is illustrated in Figure 34.12.

The most well-known application of dynamic CT can probably be found in medical CT (see also Section III, Chapter 41, for 4D CT diagnostic imaging). The motion of the heart and/or lungs cause tissue to deform during the imaging process, making the tomography problem a dynamic one (Nehmeh and Erdi 2008). In gated CT, projections are sorted into several phase bins, and a reconstruction is generated separately for every separate phase bin. The sorting is typically performed with an external breathing or electrocardiogram (ECG) signal (Low et al. 2003; Vedam et al. 2003; Nieman 2014a). In order to improve reconstruction quality, the correlation of reconstructions at adjacent phases can be exploited by temporal regularization (Jia et al. 2010; Gao et al. 2011). Approaches without gating typically incorporate motion models into the reconstruction algorithm (Rit et al. 2009; Van Eyndhoven et al. 2012; Van Nieuwenhove et al. 2017). Another medical dynamic CT application is perfusion CT, where a contrast bolus is injected into the patient's blood stream and the local concentration changes in an organ of interest (brain, lung, liver, etc.) are monitored (Miles and Griffiths 2003). The same type of dynamic problems are naturally also encountered in small animal imaging (Schambach et al. 2010).

Dynamic CT problems are also frequently encountered in material research. In pressure tests, an incrementally increasing pressure is applied to a sample, while simultaneously monitoring the changes inside the sample (Shi et al. 1999; Elliott et al. 2002; Landis et al. 2006). Rigid sample motion, causing the projections to be misaligned, or affine deformation (scaling and rotation) is a typical problem encountered in X-ray imaging.

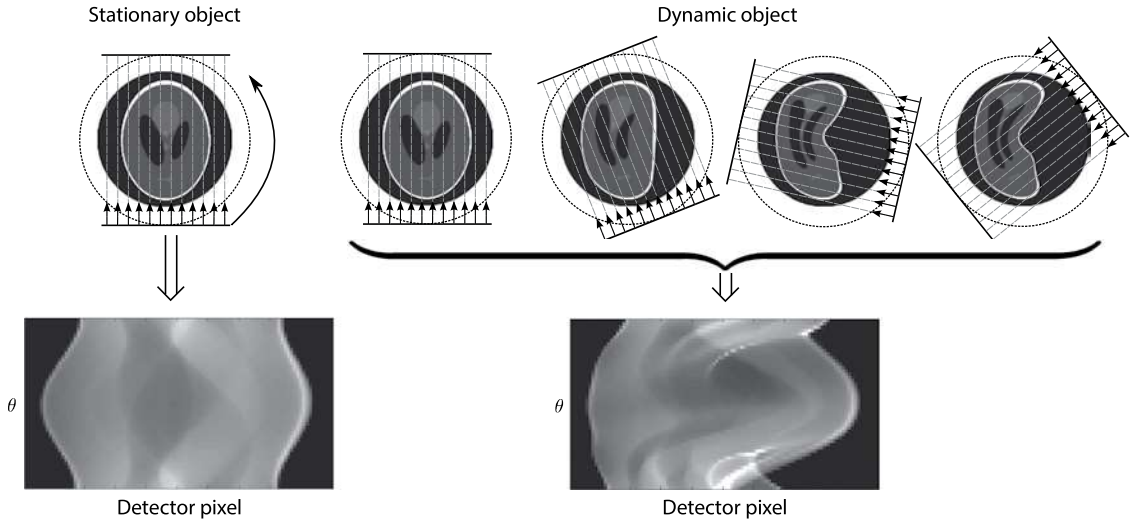

FIGURE 34.12 The effect of a time-varying object on the sinogram, illustrated with the Shepp–Logan phantom. In the left part of the figure, the sinogram corresponding to a stationary object is visualized. In the right part of the figure, the effect of a deformation in the same object on the sinogram is illustrated.

Fortunately, solutions exist to estimate affine deformations, without the need for a computational intensive iterative reconstruction scheme (Nieuwenhove et al. 2017). Other examples of dynamic CT include sample changes (while scanning) due to radiation damage (Luther 2007; Stern et al. 2009), the monitoring of root growth over time (Tracy et al. 2010), imaging the solar corona (Butala et al. 2010), the investigation of micro-structural changes during development of internal flesh browning of apples (Herremans et al. 2013), etcetera.

When dealing with time-varying objects, an extra dependency on time is introduced. Therefore, the object's attenuation coefficient function is represented by $f(x, y, t)$. The projection value model of Equation 34.29, hence, also includes the time dependency, i.e.,

$$p_i = \int_{-\frac{\Delta r}{2}}^{\frac{\Delta r}{2}} \int_{L(t_i,\theta_i)} f(x,y,t_i)\,ds\,dr' \tag{34.73}$$

where t_i represents the point in time at which the ith projection value was acquired.

In the algebraic setting, the dynamic object is typically represented as a time series of images, $\boldsymbol{x}_r \in \mathbb{R}^N$, where each $r \in \{1, \ldots, R\}$ is the index referring to a particular point in time (i.e., a *time frame*), and R is the total number of time frames. The entire time series is represented by the vertical concatenation of $\boldsymbol{x}_1, \boldsymbol{x}_2, \ldots, \boldsymbol{x}_R$, such as, $\tilde{\boldsymbol{x}} := (\boldsymbol{x}_1^T, \boldsymbol{x}_2^T, \ldots, \boldsymbol{x}_R^T)^T \in \mathbb{R}^{RN}$. To reconstruct this time series of images, projection data is acquired for each time frame by rotating source and detector multiple times around the object, or, equivalently, by rotating the object itself in between a fixed source and detector. Standard approaches then typically reconstruct the object at each time frame individually, solely based on the projection data corresponding to a single 180° or 360° rotation. For every $r \in \{1, \ldots, R\}$, let $\boldsymbol{p}_r \in \mathbb{R}^M$ be the measured projection data corresponding to the rth time frame. Define $\boldsymbol{W} \in \mathbb{R}^{RM \times N}$ as the forward projection matrix that models all projection angles, and $\boldsymbol{W}_r \in \mathbb{R}^{M \times N}$ as the sub-matrix of $\boldsymbol{W}$ that models the forward projection for the rth time frame. Furthermore, let the full vector of measured projection data, $\tilde{p} \in \mathbb{R}^{RM}$, be the vertical concatenation of $\boldsymbol{p}_1, \boldsymbol{p}_2, \ldots, \boldsymbol{p}_R$, and $\tilde{\boldsymbol{W}}$ the block diagonal matrix consisting of blocks $\boldsymbol{W}_1, \boldsymbol{W}_2 \ldots \boldsymbol{W}_R$. In summary, we have introduced the following notations:

$$\tilde{\boldsymbol{W}} := \begin{bmatrix} \boldsymbol{W}_1 & 0 & \cdots & 0 \\ 0 & \boldsymbol{W}_2 & & 0 \\ \vdots & & \ddots & \vdots \\ 0 & 0 & \cdots & \boldsymbol{W}_R \end{bmatrix} \in \mathbb{R}^{RM \times RN}, \quad \boldsymbol{W} := \begin{bmatrix} \boldsymbol{W}_1 \\ \boldsymbol{W}_2 \\ \vdots \\ \boldsymbol{W}_R \end{bmatrix} \in \mathbb{R}^{RM \times N} \tag{34.74}$$

and

$$\tilde{\boldsymbol{p}} := \begin{bmatrix} \boldsymbol{p}_1 \\ \boldsymbol{p}_2 \\ \vdots \\ \boldsymbol{p}_R \end{bmatrix} \in \mathbb{R}^{RM}, \quad \tilde{\boldsymbol{x}} := \begin{bmatrix} \boldsymbol{x}_1 \\ \boldsymbol{x}_2 \\ \vdots \\ \boldsymbol{x}_R \end{bmatrix} \in \mathbb{R}^{RN} \tag{34.75}$$

Analogously to the reconstruction problem for the static case, the goal in dynamic tomography is to find a reconstruction $\tilde{x}$ that minimizes

$$\left\| \tilde{\boldsymbol{W}}\tilde{\boldsymbol{x}} - \tilde{\boldsymbol{p}} \right\| \tag{34.76}$$

for some norm $\|\cdot\|$. If only a few projections are available per time frame, finding $\tilde{\boldsymbol{x}}$ such that Equation 34.76 is minimal represents an ill-posed problem. This is mainly due to the large null space of the forward operator, $\tilde{\boldsymbol{W}}$, and the noise in the measured projection data, $\tilde{\boldsymbol{p}}$. Therefore, directly minimizing Equation 34.76 for $\tilde{\boldsymbol{x}}$ (e.g., by applying SIRT separately to the projection data, $\boldsymbol{p}_r$, for $r = 1, \ldots, R$) will typically result in a solution $\tilde{\boldsymbol{x}}$, which is fully dominated by noise. This problem can be alleviated by imposing constraints/models on the reconstruction, $\tilde{\boldsymbol{x}}$, resulting

in a smaller solution space. The connection between the different time frames, $\boldsymbol{x}_r$ (with $r = 1, \ldots, R$), is modeled, thereby basically reducing the degrees of freedom for the reconstruction algorithm in a model-compliant manner. The more accurately modeled reconstruction problem results in solutions that are less dominated by artifacts and more accurately represent the true underlying solution.

As was suggested in the previous paragraph, modeling the connection between the different time frames can be beneficial. If the information from reconstructions at different time frames is combined, it becomes important to avoid redundant information as much as possible. This can be achieved by changing the conventional acquisition angle selection schemes to more advanced. In what follows, three different ways of selecting the acquisition angles for the projection data corresponding to each time frame are introduced. Let M_t denote the number of projections acquired per time frame, and M_d the number of detector elements per projection (this implies that the total number of projection values per time frame is given by $M = M_t M_d$). Next, denote the projection angle for the lth projection as ω_l ($l = 1, \ldots, M_t R$). This notation allows us to define the following three angle selection schemes, which are visualized in Figure 34.13:

1. *Conventional decomposition*: For each 180° rotation, the same (equiangular) projection angles are selected. This approach is the most widely used and suffices if the scanned object is reconstructed independently at each time frame. The angles are selected as follows:

$$\omega_l = (l-1)\omega_\Delta \quad l = 1,\ldots,M_t R \tag{34.77}$$

where $\omega_\Delta = \pi/M_t$. This angle selection scheme is illustrated in Figure 34.13a.

2. *Binary decomposition*: Analogously to the conventional decomposition, the acquisition angles in each 180° rotation are chosen equiangularly. However, a small angular shift is applied to the starting angle after each 180° rotation. The first M_t equiangular projection angles are chosen as $\omega_l = (l-1)\omega_\Delta \in [0, \pi - \omega_\Delta]$ for $l = 1, \ldots, M_t$. The other projection directions are defined as

$$\omega_k M_t + l = k(\pi - \omega_\Delta) + k\frac{\pi}{R} + (l-1)\omega_\Delta \tag{34.78}$$

for $l = 1, \ldots, M_t$, $k = 1, \ldots, \lfloor R/M_t \rfloor$ and $kM_t + l \leq M_t R$. The angles $\omega_1, \omega_2, \ldots, \omega_2 M_t$ are schematically displayed in Figure 34.13b. The small incremental step, $k\frac{\pi}{R}$, in Equation 34.78 ensures that there exist no two projection directions that are equal modulo π. This is beneficial for reconstruction algorithms that aim at combining information from different time frames. On the one

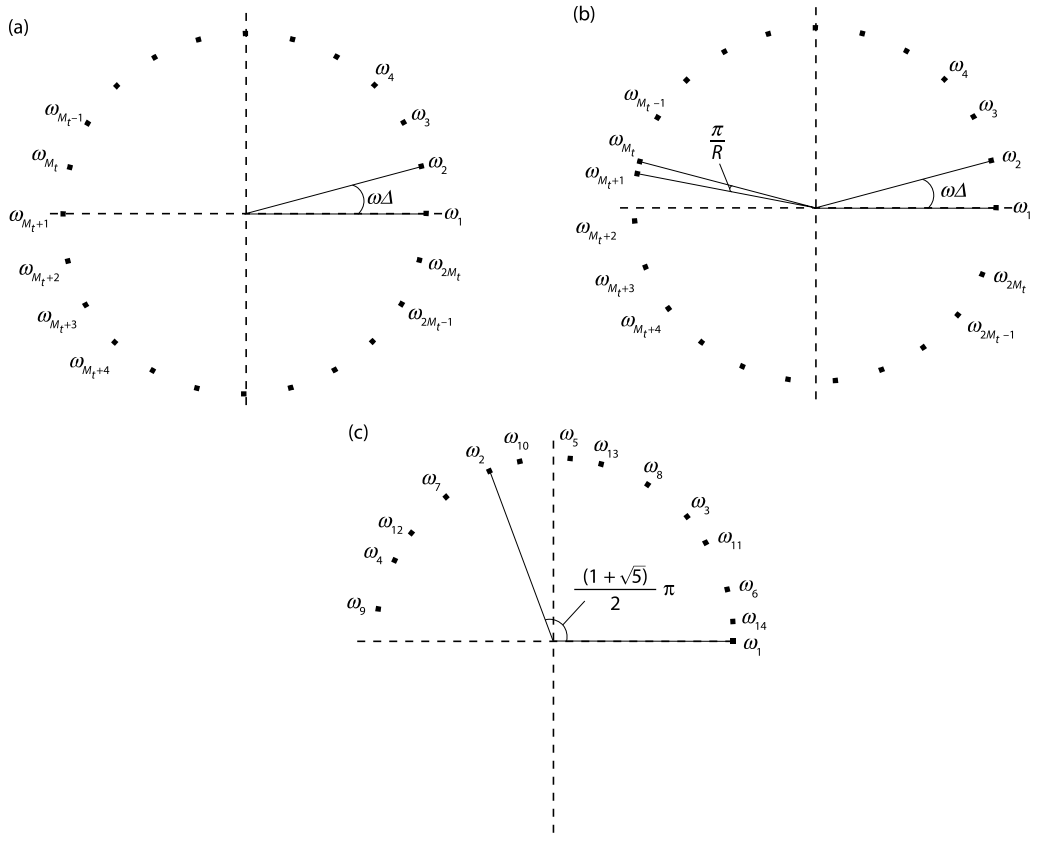

FIGURE 34.13 Illustration of three different approaches to select the acquisition angles in dynamic CT. (a) Conventional decomposition, (b) binary decomposition, (c) golden ratio decomposition.

hand, using the same projection angle (modulo π for parallel beam and modulo 2π for fan beam) more than once increases the signal-to-noise ratio (SNR). On the other hand, this will introduce redundant angular information, since the rays going through stationary regions (that is, regions inside the object that do not change over time) give the same projection values (up to noise). This situation is avoided by choosing the projection angles via Equation 34.78. Furthermore, Equation 34.78 guarantees that each subsequent M_t projection directions cover a range of approximately 180°, thus avoiding limited view artifacts.

3. *Golden ratio decomposition*: In the "golden ratio" scanning scheme, source and detector are rotated over a fixed angular step of $\Delta\omega = \pi(1+\sqrt{5})/2$ radians to determine the next acquisition angle (Kohler 2004; Kaestner et al. 2011). More precisely, the projection angle, ω_l ($l = 1, \ldots, RM_t$), is defined by

$$\omega_l = \left((l-1)\frac{\left(1+\sqrt{5}\right)}{2}\pi \right) \bmod \pi$$

In the binary decomposition, the user must select the number of projections per time frame before the experiment starts. The golden ratio scanning scheme is more flexible in the sense that it allows the user to select an arbitrary number of projections per time frame after the data acquisition, while still approximately covering equiangular positions over the entire angular range for each time frame (Kaestner et al. 2011). This allows the user to balance the temporal and spatial resolution *a posteriori*, which is a useful property in many applications. Furthermore, the golden ratio decomposition also ensures that the same projection angle is never selected twice.

34.5 Conclusion

X-ray CT allows one to visualize the interior of objects by acquiring a set of radiographs (projections) and reconstructing an image from this set of measured projections. Fast analytic reconstruction methods exist based on filtered back projection. However, they only generate high quality reconstructions if many projections are available from all angles. If not, one can resort to computationally more intensive (and, hence, slower), iterative reconstruction methods that often lead to much better image quality, certainly if appropriate prior knowledge is exploited. The most common iterative reconstruction methods have been reviewed and discussed in this chapter.

REFERENCES

Andersen, A.H. and A.C. Kak. 1984. Simultaneous algebraic reconstruction technique (SART): A superior implementation of the ART algorithm. *Ultrasonic Imaging* 6:81–94.

Anoop, K.P. and K. Rajgopal. 2009. Image reconstruction with laterally truncated projections in helical cone-beam CT: Linear prediction based projection completion techniques. *Computerized Medical Imaging and Graphics* 33:283–94.

Batenburg, K.J. and L. Plantagie. 2012. Fast approximation of algebraic reconstruction methods for tomography. *IEEE Transactions on Image Processing* 21:3648–58.

Batenburg, K.J. and J. Sijbers. 2011. DART: A practical reconstruction algorithm for discrete tomography. *IEEE Transactions on Image Processing* 20:2542–53.

Bushberg, J.T., J.A. Seibert, E.M. Leidholdt, and J.M. Boone. 2011. *The Essential Physics of Medical Imaging*, 3rd edn, ch. 3. Lippincott Williams & Wilkins.

Butala, M.D., R.J. Hewett, R.A. Frazin, and F. Kamalabadi. 2010. Dynamic three-dimensional tomography of the solar corona. *Solar Physics* 262:495–509.

Buzug, T.M. 2008. *Computed Tomography: From Photon Statistics to Modern Cone-Beam CT*. Springer-Verlag.

Cant, J., W.J. Palenstijn, G. Behiels, and J. Sijbers. 2015. Modeling blurring effects due to continuous gantry rotation: Application to region of interest tomography. *Medical Physics* 42:2709–17.

Chambolle, A. 2004. An algorithm for total variation minimization and applications. *Journal of Mathematical Imaging and Vision* 20:89–97.

Dabravolski, A., K.J. Batenburg, and J. Sijbers. 2014. A multiresolution approach to discrete tomography using DART. *PloS ONE* 9:1–10.

Duisterwinkel, H.A., J.K. van Abbema, M.J. van Goethem, R. Kawachimaru, L. Pa-ganini, E.R. van der Graaf, and S. Brandenburg. 2015. Spectra of clinical CT scanners using a portable Compton spectrometer. *Medical Physics* 42:1884–94.

Elliott, J., A. Windle, J. Hobdell, G. Eeckhaut, R. Oldman, W. Ludwig, E. Boller, P. Cloetens, and J. Baruchel. 2002. In-situ deformation of an open-cell flexible polyurethane foam characterised by 3d computed microtomography. *Journal of Materials Science* 37:1547–55.

Feldkamp, L.A., L.C. Davis, and J.W. Kress. 1984. Practical cone-beam algorithm. *Journal of the Optical Society of America A* 1:612–19.

Gao, H., J.-F. Cai, Z. Shen, and H. Zhao. 2011. Robust principal component analysis-based four-dimensional computed tomography. *Physics in Medicine and Biology* 56:3181–98.

Gordon, R., R. Bender, and G.T. Herman. 1970. Algebraic Reconstruction Techniques (ART) for three-dimensional electron microscopy and X-ray photography. *Journal of Theoretical Biology* 29:471–81.

Gregor, J. and T. Benson. 2008. Computational analysis and improvement of SIRT. *IEEE Transactions on Medical Imaging* 27:918–24.

Guan, H. and R. Gordon. 1994. A projection access order for speedy convergence of ART (algebraic reconstruction technique): A multilevel scheme for computed tomography. *Physics in Medicine and Biology* 39:2005.

Guan, Y., Y. Gong, W. Li, J. Gelb, L. Zhang, G. Liu, X. Zhang, X. Song, C. Xia, Y. Xiong, H. Wang, Z. Wu, and Y. Tian. 2011. Quantitative analysis of micro structural and conductivity evolution of Ni-YSZ anodes during thermal cycling based on nano-computed tomography. *Journal of Power Sources* 196:10601–5.

Heideman, M., D. Johnson, and C. Burrus. 1984. Gauss and the history of the fast fourier transform. *ASSP Magazine, IEEE* 1:14–21.

Hemberg, O., M. Otendal, and H. Hertz. 2003. Liquid-metal-jet anode electron-impact X-ray source. *Applied Physics Letters* 83:1483–5.

Herman, G.T. and A. Kuba. 2008. *Advances in Discrete Tomography and Its Applications*. Bazel, Zwitserland: Springer Science & Business Media.

Herremans, E., P. Verboven, E. Bongaers, P. Estrade, B.E. Verlinden, M. Wevers, M.L. Hertog, and B.M. Nicolai. 2013. Characterisation of braeburn browning disorder by means of x-ray micro-CT. *Postharvest Biology and Technology* 75:114–24.

Hsung, T.-C. and D. Lun. 2000. New sampling scheme for region-of-interest tomography. *IEEE Transactions on Signal Processing* 48:1154–63.

Hudson, H.M. and R.S. Larkin. 1994. Accelerated image reconstruction using ordered subsets of projection data. *IEEE Transactions on Medical Imaging* 13:601–9.

Jia, X., Y. Lou, B. Dong, Z. Tian, and S. Jiang. 2010. 4D computed tomography reconstruction from few-projection data via temporal non-local regularization. *Medical Image Computing and Computer Assisted Intervention (MICCAI)* 13:143–50.

Jiang, M. and G. Wang. 2003. Convergence studies on iterative algorithms for image reconstruction. *IEEE Transactions on Medical Imaging* 22:569–79.

Joseph, P.M. 1982. An improved algorithm for reprojecting rays through pixel images. *IEEE Transactions on Medical Imaging* 1:192–6.

Kaestner, A., B. Munch, T. Pavel, and L. Butler. 2011. Spatiotemporal computed tomography of dynamic processes. *Optical Engineering* 50:123201.

Kak, A.C. and M. Slaney. 2001. *Principles of Computerized Tomographic Imaging*. New York: Society of Industrial and Applied Mathematics.

Kelcz, F., P.M. Joseph, and S. K. Hilal. 1979. Noise considerations in dual energy CT scanning. *Medical Physics* 6:418–25.

Kohler, T. 2004. A projection access scheme for iterative reconstruction based on the golden section. *Nuclear Science Symposium Conference Record* 6:3961–5.

Kudo, H., T. Rodet, F. Noo, and M. Defrise. 2004. Exact and approximate algorithms for helical cone-beam CT. *Physics in Medicine and Biology* 49:2913.

Landis, E.N., T. Zhang, E.N. Nagy, G. Nagy, and W.R. Franklin. 2006. Cracking, damage and fracture in four dimensions. *Materials and Structures* 40:357–64.

Lange, K. and R. Carson. 1984. EM reconstruction algorithms for emission and transmission tomography. *Journal of Computer Assisted Tomography* 8:306–16.

Lange, K. and J. Fessler. 1995. Globally convergent algorithms for maximum a posteriori transmission tomography. *IEEE Transactions on Image Processing* 4:1430–8.

Lange, K., M. Bahn, and R. Little. 1987. A theoretical study of some maximum likelihood algorithms for emission and transmission tomography. *IEEE Transactions on Medical Imaging* 6:106–14.

Lou, Y., X. Zhang, S. Osher, and A. Bertozzi. 2010. Image recovery via nonlocal operators. *Journal of Scientific Computing* 42:185–97.

Low, D.A., M. Nystrom, E. Kalinin, P. Parikh, J.F. Dempsey, J.D. Bradley, S. Mutic, S.H. Wahab, T. Islam, G. Christensen, D.G. Politte, and B.R. Whiting. 2003. A method for the reconstruction of four-dimensional synchronized CT scans acquired during free breathing. *Medical Physics* 30:1254.

Luther, P.K. 2007. Sample shrinkage and radiation damage of plastic sections. In *Electron Tomography*. 2nd edition, edited by J. Frank, ch. 1, 17–48. New York, NY: Springer.

Matej, S. and R. Lewitt. 1992. Image representation and tomographic reconstruction using spherically-symmetric volume elements. In *Nuclear Science Symposium and Medical Imaging Conference, 1992, Conference Record of the 1992 IEEE*, vol. 2, 1191–3, Orlando, FL, October 25–31, 1992.

Meyer, E., R. Raupach, M. Lell, B. Schmidt, and M. Kachelrieß. 2010. Normalized metal artifact reduction (NMAR) in computed tomography. *Medical Physics* 37:5482–93.

Meyer, E., R. Raupach, M. Lell, B. Schmidt, and M. Kachelrieß. 2012. Frequency split metal artifact reduction (FSMAR) in computed tomography. *Medical Physics* 39:1904–16.

Miles, K.A. and M.R. Griffiths. 2003. Perfusion CT: A worthwhile enhancement? *The British Journal of Radiology* 76:220–31.

Nehmeh, S.A. and Y.E. Erdi. 2008. Respiratory motion in positron emission tomography/computed tomography: A review. *Seminars in Nuclear Medicine* 38:167–76.

Nieuwenhove, V.V., J.D. Beenhouwer, T.D. Schryver, L.V. Hoorebeke, and J. Sijbers. 2017. Image quality assessment: From error visibility to structural similarity. *IEEE Transactions on Image Processing* 26:1441–51.

Paige, C.C. and M.A. Saunders. 1982. LSQR: An algorithm for sparse linear equations and sparse least squares. *ACM Transactions on Mathematical Software* 8:43–71.

Pelt, D.M. and K.J. Batenburg. 2013. Fast tomographic reconstruction from limited data using artificial neural networks. *IEEE Transactions on Image Processing* 22:5238–51.

Rit, S., D. Sarrut, and L. Desbat. 2009. Comparison of analytic and algebraic methods for motion-compensated cone-beam CT reconstruction of the thorax. *IEEE Transactions on Medical Imaging* 28:1513–25.

Rockmore, A. and A. Macovski. 1977. A maximum likelihood approach to transmission image reconstruction from projections. *IEEE Transactions on Nuclear Science* 24:1929–35.

Roelandts, T., K.J. Batenburg, E. Biermans, C. Kübel, S. Bals, and J. Sijbers. 2012. Accurate segmentation of dense nanoparticles by partially discrete electron tomography. *Ultramicroscopy* 114:96–105.

Röntgen, W.C. 1898. Über eine neue art von strahlen. *Annalen der Physik* 300:1–11.

Schambach, S.J., S. Bag, L. Schilling, C. Groden, and M.A. Brockmann. 2010. Application of micro-CT in small animal imaging. *Methods* 50:2–13.

Schlomka, J.P., E. Roessl, R. Dorscheid, S. Dill, G. Martens, T. Istel, C. Bäumer, C. Herrmann, R. Steadman, G. Zeitler, A. Livne, and R. Proksa. 2008. Experimental feasibility of multi-energy photon-counting k-edge imaging in pre-clinical computed tomography. *Physics in Medicine and Biology* 53:4031.

Shepp, L.A. and B.F. Logan. 1974. The Fourier reconstruction of a head section. *IEEE Transactions on Nuclear Science* 21:21–43.

Shi, B., Y. Murakami, Z. Wu, J. Chen, and H. Inyang. 1999. Monitoring of internal failure evolution in soils using computerization X-ray tomography. *Engineering Geology* 54:321–8.

Sidky, E.Y., D.N. Kraemer, E.G. Roth, C. Ullberg, I.S. Reiser, and X. Pan. 2014. Analysis of iterative region-of-interest image reconstruction for X-ray computed tomography. *Journal of Medical Imaging* 1:031007.

Stern, E.A., Y. Yacoby, G.T. Seidler, K.P. Nagle, M.P. Prange, A.P. Sorini, J.J. Rehr, and A. Joachimiak. 2009. Reducing radiation damage in macromolecular crystals at synchrotron sources. *Acta Crystallographica. Section D, Biological Crystallography* 65:366–74.

Tang, J., B.E. Nett, and G.-H. Chen. 2009. Performance comparison between total variation (TV)-based compressed sensing and statistical iterative reconstruction algorithms. *Physics in Medicine and Biology* 54:5781.

Tracy, S.R., J.A. Roberts, C.R. Black, A. McNeill, R. Davidson, and S.J. Mooney. 2010. The X-factor: Visualizing undisturbed root architecture in soils using X-ray computed tomography. *Journal of Experimental Botany* 61, 311–13.

van Aarle, W., K.J. Batenburg, and J. Sijbers. 2011. Optimal threshold selection for segmentation of dense homogeneous objects in tomographic reconstructions. *IEEE Transactions on Medical Imaging* 30:980–9.

van Aarle, W., W.J. Palenstijn, J. Cant, E. Janssens, F. Bleichrodt, A. Dabravolski, J. De Beenhouwer, and J. Sijbers. 2016. Fast and flexible X-ray tomography using the ASTRA toolbox. *Optics Express* 24:25129–47.

van Aarle, W., W.J. Palenstijn, J. De Beenhouwer, T. Altantzis, S. Bals, K.J. Batenburg, and J. Sijbers. 2015. The ASTRA Toolbox: A platform for advanced algorithm development in electron tomography. *Ultramicroscopy* 157:35–47.

Van Eyndhoven, G., J. Sijbers, and K.J. Batenburg. 2012. Combined motion estimation and reconstruction in tomography. In *Computer Vision ECCV 2012. Workshops and Demonstrations, vol. 7583 of Lecture Notes in Computer Science*, edited by A. Fusiello, V. Murino, and R. Cucchiara pp, 12–21. Berlin, Heidelberg, Germany: Springer.

Van Nieuwenhove, V., J. De Beenhouwer, J. Vlassenbroeck, M. Brennan, and J. Sijbers. 2017. MoVIT: A tomographic reconstruction framework for 4D-CT. *Optics Express* 25(16):19236–50.

Van Nieuwenhove, V., J. De Beenhouwer, T. De Schryver, L. Van Hoorebeke, and J. Sijbers. 2017. Data-driven affine deformation estimation and correction in cone beam computed tomography. *IEEE Transactions on Image Processing* 26:1441–51.

Vedam, S.S., P.J. Keall, V.R. Kini, H. Mostafavi, H.P. Shukla, and R. Mohan. 2003. Acquiring a four-dimensional computed tomography dataset using an external respiratory signal. *Physics in Medicine and Biology* 48:45–62.

Winick, H. 1995. *Synchrotron Radiation Sources: A Primer.* Vol. 1. Singapore: World Scientific.

Zhang, X., M. Burger, X. Bresson, and S. Osher. 2010. Bregmanized nonlocal regularization for deconvolution and sparse reconstruction. *SIAM Journal on Imaging Sciences* 3:253–76.